

Orographic flow-blocking scheme characteristics

By A. R. BROWN* and S. WEBSTER
Met Office, Exeter, UK

(Received 9 March 2004; revised 28 June 2004)

SUMMARY

The characteristics of the orographic flow blocking parametrization used in the Met Office Unified Model are examined in a one-dimensional framework. This approach allows feedback of the parametrized stresses on the winds resulting, in some cases, in stresses very different from those that would be obtained without this feedback. The key controlling non-dimensional parameters are identified, and the implications of the results for the use of the scheme in climate and numerical weather-prediction models are discussed.

KEYWORDS: Orography Parametrization

1. INTRODUCTION

The performance of large-scale numerical weather-prediction (NWP) and climate models is highly sensitive to the representation of the effects of unresolved orography. Early schemes (e.g. Palmer *et al.* 1986; McFarlane 1987) showed beneficial effects from parametrizing the drag associated with the breaking of linear hydrostatic gravity waves. Most of the drag from these schemes was deposited in the lower stratosphere. This had a direct impact on the stratospheric jets, and also an indirect effect on the surface winds through induced secondary circulations.

More recent schemes (e.g. see the review by Kim *et al.* 2003) have attempted to represent a variety of additional drag mechanisms such as hydraulic jumps, trapped lee waves and boundary-layer turbulent form drag. In general the trend has been towards increased low-level and reduced upper-level drag. A key step in this process has been the introduction of explicit parametrizations of the effects of orographic flow blocking (Lott and Miller 1997; Scinocca and McFarlane 2000; Webster *et al.* 2003). While these schemes differ in detail, they all provide significant drag below the height of the top of the unresolved orography. For example, Webster *et al.* noted that, with their scheme, the zonal mean surface stress associated with flow blocking was typically three times larger than that associated with propagating gravity waves. Another important characteristic which these schemes share is that the surface stress depends on winds which are themselves directly affected by the flow-blocking scheme. In this respect the schemes are more akin to boundary-layer schemes than to traditional gravity-wave schemes (in which the surface stress depends on low-level winds which are affected only indirectly by the upper-level drag).

One consequence of the direct feedbacks between the winds and stresses in any blocked layer is that it is not trivial to predict what the parametrized drag will be, even when a known upstream flow impinges on a grid box in which the flow-blocking scheme is active. Similarly, a change to some aspect of a scheme's formulation (e.g. to the magnitude of a tuning coefficient) may lead to changes in stresses quite different to those that would be obtained if the winds remained unchanged. The complex dependence of the parametrized drag on the wind speed in the blocked layer also opens up the possibility of having multiple solutions.

In view of the complex behaviour described above, and of the practical importance of orographic flow-blocking schemes, the aim of this paper is to provide further insights

* Corresponding author: Met Office, FitzRoy Road, Exeter, Devon EX1 3PB, UK.

e-mail: andy.brown@metoffice.gov.uk

© Crown copyright, 2004.

into the properties and behaviour of one of these schemes. This will be done in an idealized framework by examining the equilibrium solutions of a one-dimensional (1D) model incorporating the Webster *et al.* (2003) blocking parametrization in addition to Coriolis terms and an imposed large-scale pressure gradient. This model is detailed in section 2, and the solutions are described in section 3. Section 4 examines the stability of the solutions, and section 5 discusses the relevance and implications of the results for NWP and climate modelling. Finally conclusions are given in section 6.

2. THE MODEL

We consider the 1D problem, in which the evolution of the wind components, u and v , within the blocked layer are governed by

$$\frac{\partial u(z)}{\partial t} = f(v - v_g) + \frac{\partial \tau_x(z)}{\partial z} \quad (1)$$

$$\frac{\partial v(z)}{\partial t} = -f(u - u_g) + \frac{\partial \tau_y(z)}{\partial z}. \quad (2)$$

Here f is the Coriolis parameter, and u_g and v_g are the height-independent geostrophic wind components. In this simple model, the stresses τ_x and τ_y are assumed to be solely those associated with flow blocking i.e. the influence of a separate boundary-layer scheme is not considered. Note that for convenience a Boussinesq framework is being used, and mention of density is suppressed (so that the stresses have units of m^2s^{-2}).

In the scheme of Webster *et al.* (2003), the surface values of τ_x and τ_y depend on the wind and Brunt–Väisälä frequency, N , averaged over an assumed subgrid hill height, h . The stress is then deposited linearly over this same height. Hence no shear will be introduced within the blocked layer, and we effectively have a simple one-layer model for wind below h . Considering a case where the subgrid orography is isotropic and using the Webster *et al.* parametrization, the equations for the evolution of the wind components are

$$\frac{\partial u}{\partial t} = f(v - v_g) - \frac{aN}{h}u \times \max \left[\left\{ 1 - \left(\frac{Fr}{Fr_c} \right)^2 \right\}, 0 \right], \quad (3)$$

$$\frac{\partial v}{\partial t} = -f(u - u_g) - \frac{aN}{h}v \times \max \left[\left\{ 1 - \left(\frac{Fr}{Fr_c} \right)^2 \right\}, 0 \right]. \quad (4)$$

Here $Fr = s/(Nh) = (u^2 + v^2)^{1/2}/(Nh)$ is a Froude number and s is the wind speed, and the blocking parametrization switches off when it exceeds a critical value, Fr_c . For $Fr/Fr_c < 1$, the blocking stress is proportional to a (units of m), which is the product of the mean square slope of the subgrid orography and a length-scale, \widehat{K}^{-1} , which is regarded as a tunable parameter.

Without loss of generality, we can set v_g to zero. We then solve Eqs. (3) and (4) for cases with $Fr/Fr_c < 1$, with the tendency terms set to zero, to obtain the equilibrium solution $(u, v) = (u^e, v^e)$, and s^e is the corresponding equilibrium wind speed. Dividing one equation by the other quickly leads to

$$\left(\frac{v^e}{u_g} \right)^2 = \left(\frac{u^e}{u_g} \right) - \left(\frac{u^e}{u_g} \right)^2 \quad (5)$$

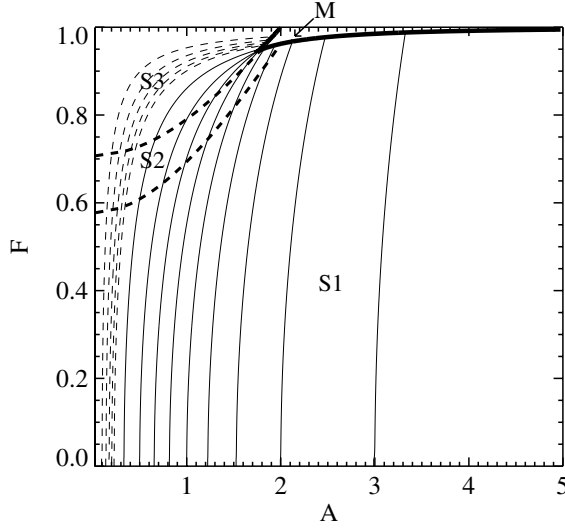


Figure 1. Solutions for u^e/u_g as a function of non-dimensional numbers A and F (see text). The heavy solid contour separates the small region of parameter space (M) exhibiting multiple solutions for u^e/u_g from the region where the cubic equation has only one real root (S). In this latter region, contours of the solution are plotted (light solid lines for $u^e/u_g = 0.1(0.1)0.9$ and dashed lines for $u^e/u_g = 0.95(0.01)0.99$). The heavy dashed lines subdivide region S into S1, S2 and S3 according to the stability of the solution, as described in section 4.

and substituting for $v = v^e$ in Eq. (3) and rearranging leads to

$$\left(\frac{Fr_g}{Fr_c}\right)^4 \left(\frac{u^e}{u_g}\right)^3 - 2 \left(\frac{Fr_g}{Fr_c}\right)^2 \left(\frac{u^e}{u_g}\right)^2 + \left\{1 + \left(\frac{fh}{aN}\right)^2\right\} \left(\frac{u^e}{u_g}\right) - \left(\frac{fh}{aN}\right)^2 = 0, \quad (6)$$

where $Fr_g = u_g/(Nh)$. Equation (6) is a cubic equation for (u^e/u_g) , with the solution depending only on the non-dimensional numbers $F = (Fr_g/Fr_c)$ and $A = (aN/fh)$. As (v^e/u_g) depends only on (u^e/u_g) (from Eq. (5)), it too must be a function of F and A .

The equilibrium surface stress components are obtained through

$$\frac{\tau_{x0}^e}{u_g^2} = \left(\frac{hf}{u_g}\right) \left(\frac{v^e}{u_g}\right), \quad (7)$$

$$\frac{\tau_{y0}^e}{u_g^2} = \left(\frac{hf}{u_g}\right) \left(1 - \frac{u^e}{u_g}\right), \quad (8)$$

and the magnitude of the surface stress, $\tau_0^e = ((\tau_{x0}^e)^2 + (\tau_{y0}^e)^2)^{1/2}$, is given by

$$\frac{\tau_0^e}{u_g^2} = \left(\frac{hf}{u_g}\right) \left(1 - \frac{u^e}{u_g}\right)^{1/2}. \quad (9)$$

Hence, normalized in this way, these stresses exhibit a dependence on a further independent non-dimensional parameter, $B = (hf/u_g)$.

3. SOLUTIONS

Equation (6) is cubic in (u^e/u_g) and may therefore have either one or multiple real roots, depending on the relative sizes of the coefficients and hence on A and F .

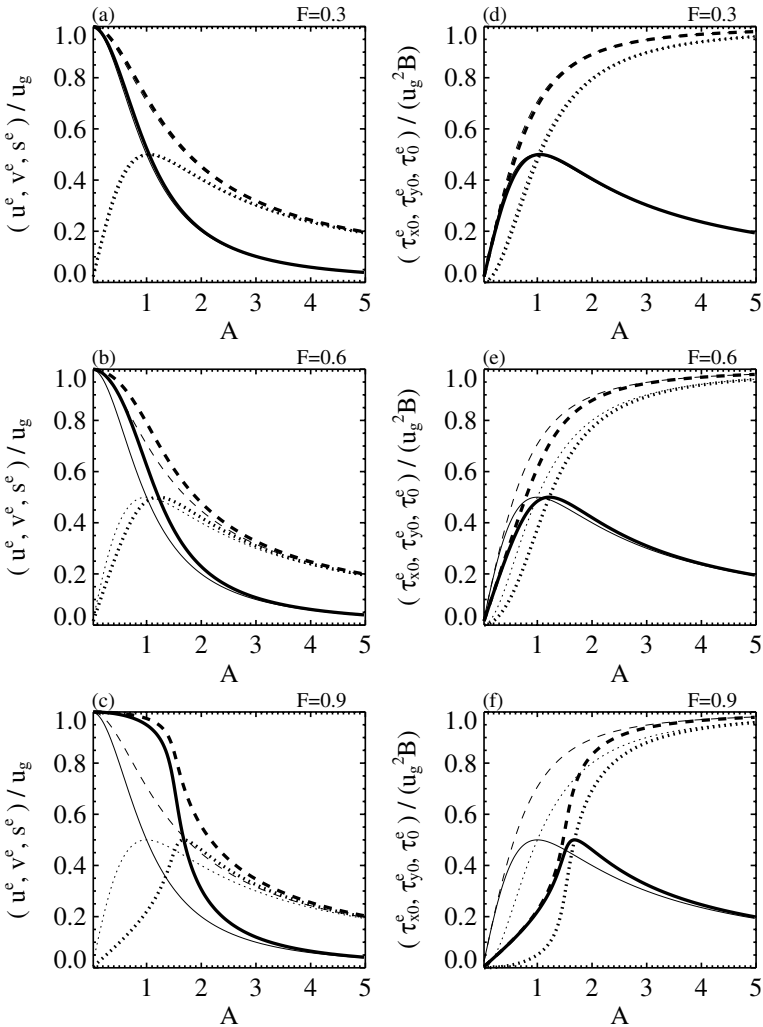


Figure 2. Solutions for u^e/u_g (solid), v^e/u_g (dotted) and $s^e/u_g = \{(u^e)^2 + (v^e)^2\}^{1/2}/u_g$ (dashed) as a function of A for (a) $F = 0.3$, (b) $F = 0.6$, and (c) $F = 0.9$. (d) to (f) are as (a) to (c), but for $\tau_{x0}^e/(u_g^2 B)$ (solid), $\tau_{y0}^e/(u_g^2 B)$ (dotted) and $\tau_0^e/(u_g^2 B)$ (dashed). The light lines show the results obtained in the $F = 0$ limit (see text), and are almost indistinguishable from the full solutions in (a) and (d).

The heavy contour in Fig. 1 indicates the boundary between the regions of parameter space which exhibit single and multiple solutions for (u^e/u_g) . While multiple solutions can be obtained, they only occur when F is close to unity and $A \gtrsim 2$, and for most of the parameter space illustrated, the cubic has a single real root. Solutions in these two parts of parameter space are now examined, starting with those in the single-root regime.

(a) *Region of parameter space with single equilibrium solution*

As well as indicating the boundary between the single and multiple solution parts of parameter space, Fig. 1 also shows contours of the solution for (u^e/u_g) in the single-solution regime. In this regime, (u^e/u_g) decreases monotonically with increasing A (for fixed F). The rate of change of (u^e/u_g) with A is a function of F . This is seen more clearly in Fig. 2(a) to (c), which show the variation of (u^e/u_g) with A (heavy

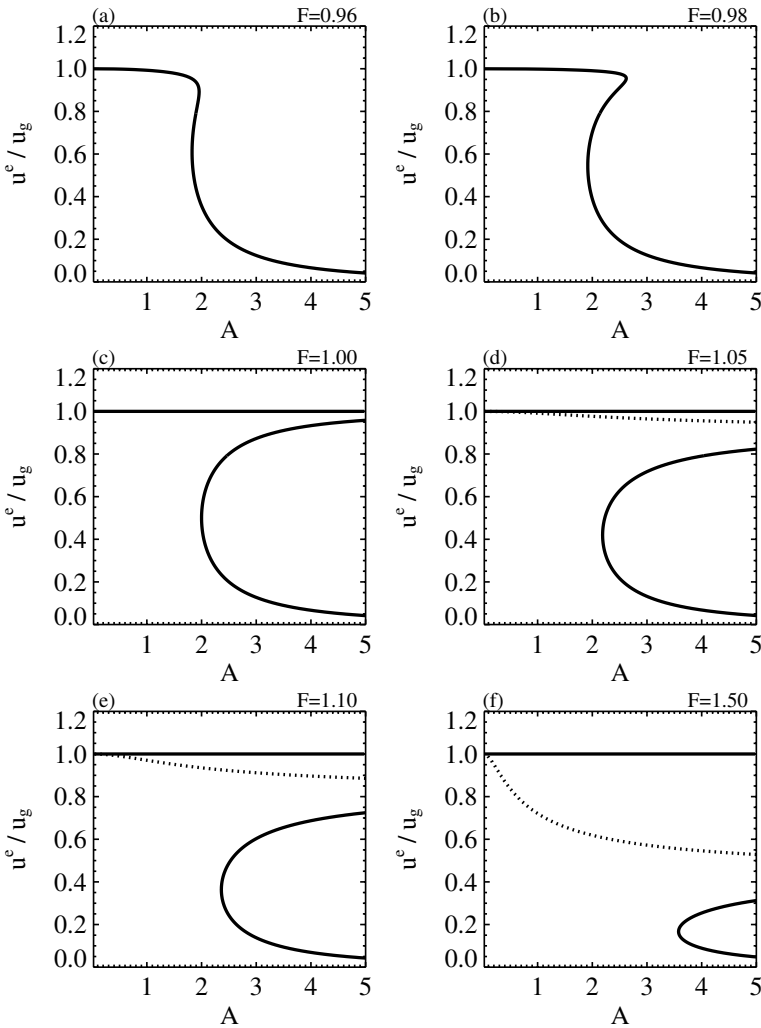


Figure 3. Solutions (solid lines) for (u^e/u_g) as a function of A for six different values of F : (a) 0.96, (b) 0.98, (c) 1.00, (d) 1.05, (e) 1.10, and (f) 1.50, all permitting multiple solutions. The dotted lines are solutions to the cubic but are not valid solutions for (u^e/u_g) as they give $Fr/Fr_c > 1$ (see text).

solid lines) at three different values of F . Additionally shown on each of these panels (light solid lines) is the solution $(u^e/u_g) = 1/(1 + A^2)$ which is obtained at $F = 0$ when the coefficients of the cubic and quadratic terms in (u^e/u_g) in Eq. (6) become zero. The $F = 0.3$ solution is almost indistinguishable from the $F = 0$ solution, and even the $F = 0.6$ solution remains reasonably close to it. However, the $F = 0.9$ solution is significantly different, with larger values of A required in order to bring about the same reduction in (u^e/u_g) . This seems intuitively reasonable as, for fixed A , the surface stress reduces as Fr approaches its critical value.

Given the solutions for (u^e/u_g) , those for (v^e/u_g) and (s^e/u_g) (dotted and dashed lines in Fig. 2(a) to (c)) immediately follow from Eq. (5). Similarly, the normalized surface stress components, $\tau_{x0}^e/(u_g^2 B)$ and $\tau_{y0}^e/(u_g^2 B)$, and the normalized magnitude of the surface stress, $\tau_0^e/(u_g^2 B)$ (shown in Fig. 2(d) to (f)) follow from Eqs. (7)–(9).

As we have seen, (u^e/u_g) decreases monotonically with increasing A for all fixed F in this regime. This means that (s^e/u_g) also decreases monotonically (as it varies as $(u^e/u_g)^{1/2}$), while $\tau_{y0}^e/(u_g^2 B)$ and $\tau_0^e/(u_g^2 B)$ increase monotonically. The angle between the wind (and surface stress) and the geostrophic wind also increases monotonically with increasing A . However, $\tau_{x0}^e/(u_g^2 B) = (v^e/u_g)$ first increases and then decreases. By differentiating Eq. (5) with respect to (u^e/u_g) , it is easily shown that the maximum value (of 0.5) occurs when $(v^e/u_g) = (u^e/u_g) = 0.5$ (for all F). However, because the relationship between (u^e/u_g) and A is a function of F , the value of $A = A_c$ at which the maximum occurs will be a function of F (as shown on Fig. 2). Substituting $(u^e/u_g) = 0.5$ into Eq. (6) and rearranging leads to

$$A_c = \frac{2}{2 - F^2}. \quad (10)$$

(b) *Region of parameter space with multiple equilibrium solutions*

Figure 2 showed the curve of the solution for (u^e/u_g) as a function of A gradually steepening as F increased from 0.3 to 0.6 to 0.9. It is the continuation of this process that leads to multiple roots when this curve goes past vertical. For example, Fig. 3(a) shows the dependence of (u^e/u_g) on A for $F = 0.96$, and it can be seen that there is a narrow range of A values that permits three solutions for (u^e/u_g) . Further increases in F towards unity increase the maximum values of A giving multiple solutions, and by $F = 1$ they are obtained for all $A \geq 2$.

Although Fig. 1 only illustrated the possibility of multiple solutions for $F \leq 1$, it is in fact also possible to obtain them for $F > 1$. In this regime, a geostrophic flow would encounter no drag, and hence $(u^e/u_g) = 1$ is clearly a solution. However, if the wind speed decreases such that Fr/Fr_c falls below unity, then blocking will occur, and an equilibrium with blocking can be obtained for some A . For example, Fig. 3 shows the results at $F = 1.05, 1.10$ and 1.50 . These have been obtained by solving the cubic for (u^e/u_g) , and then rejecting the solutions (shown dotted) with $(u^e/u_g) > 1/F^2$ which are not valid due to having $Fr/Fr_c > 1$. Two valid blocked solutions occur for all $F > 1$ as long as A exceeds some threshold, although this threshold itself increases with F .

4. STABILITY OF SOLUTIONS

Consider a small perturbation (u', v') from an equilibrium solution i.e. $(u, v) = (u^e + u', v^e + v')$. From Eqs. (3) and (4), the linearized equations for the evolution of the perturbation are

$$\frac{\partial u'}{\partial t} = f v' - \frac{aN}{h} \left(\left[1 - \frac{\{(u^e)^2 + (v^e)^2\}}{(Fr_c Nh)^2} \right] u' - 2 \frac{(u^e u' + v^e v')}{(Fr_c Nh)^2} u^e \right), \quad (11)$$

$$\frac{\partial v'}{\partial t} = -f u' - \frac{aN}{h} \left(\left[1 - \frac{\{(u^e)^2 + (v^e)^2\}}{(Fr_c Nh)^2} \right] v' - 2 \frac{(u^e u' + v^e v')}{(Fr_c Nh)^2} v^e \right). \quad (12)$$

By adding Eq. (11) multiplied by u' to Eq. (12) multiplied by v' , and rearranging, an equation is obtained for the evolution of $E = 0.5(u'^2 + v'^2)$:

$$\frac{\partial E}{\partial t} = -2fAE \left(\frac{Fr^e}{Fr_c} \right)^2 \left[\left(\frac{Fr_c}{Fr^e} \right)^2 - 1 - \frac{2(u^e u' + v^e v')^2}{\{(u^e)^2 + (v^e)^2\}(u'^2 + v'^2)} \right]. \quad (13)$$

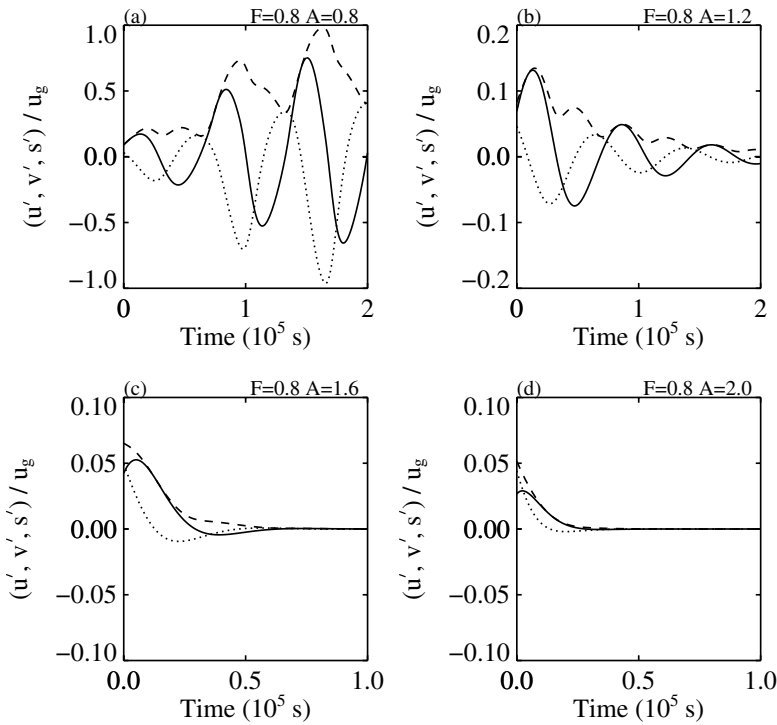


Figure 4. Evolution of u'/u_g (solid), v'/u_g (dotted) and s'/u_g (dashed) in numerical integrations of Eqs. (3) and (4) for $F = 0.8$ and four different values of A : (a) 0.8, (b) 1.2, (c) 1.6, and (d) 2.0. See text for details.

Here $Fr^e = s^e/(Nh)$ is the equilibrium Froude number. The last term on the right-hand side of Eq. (13) is equal to $2 \cos^2 \theta$, where θ is the angle between the directions of the equilibrium and perturbation velocity vectors. Therefore the requirement for the energy of the perturbation to decrease with time is that

$$\left(\frac{Fr_c}{Fr^e} \right)^2 > 1 + 2 \cos^2 \theta. \quad (14)$$

For this to be satisfied for all θ requires

$$\frac{Fr^e}{Fr_c} < \frac{1}{\sqrt{3}}, \quad (15)$$

which in turn requires $(u^e/u_g) < 1/(3F^2)$. From the cubic equation for (u^e/u_g) , this will always be satisfied for $F \leq 1/\sqrt{3}$, but for $F > 1/\sqrt{3}$ it requires $A > 1.5(3F^2 - 1)^{1/2}$. Physically this instability can be understood, since for solutions with $(Fr^e/Fr_c) > 1/\sqrt{3}$, an increase in wind leads to a decrease in drag (and vice versa).

A less stringent condition is to demand the average value of $\partial E/\partial t$ over all possible values of θ should be negative. Then, ignoring possible nonlinear effects, E will decrease over the period of an inertial oscillation, even if it is increasing at some times within that period. This requires

$$\frac{Fr}{Fr_c} < \frac{1}{\sqrt{2}}, \quad (16)$$

or equivalently $(u^e/u_g) < 1/(2F^2)$. This will always be satisfied for $F \leq 1/\sqrt{2}$, but for $F > 1/\sqrt{2}$ it requires $A > 2(2F^2 - 1)^{1/2}$.

The single-root regime in Fig. 1 is subdivided into separate subregimes (demarcated by thick dashed lines) according to the stability of the solution. In S1, $(Fr^e/Fr_c) < 1/\sqrt{3}$, and the equilibrium solution is stable. In S2, $1/\sqrt{3} \leq (Fr^e/Fr_c) < 1/\sqrt{2}$, and the energy associated with a perturbation from the equilibrium solution will decrease on average, but is not bound to at all times. In S3, $1/\sqrt{2} \leq (Fr^e/Fr_c)$, and the equilibrium is unstable.

To provide a numerical verification of the above results, a simple code was written to step Eqs. (3) and (4) in time. It was run for various A and F , starting with velocity $(u, v) = (u^e + u', v^e + v') = 1.1(u^e, v^e)$. As an example, Fig. 4 shows the evolution of $u'/u_g, v'/u_g$ and s'/u_g where $s' = (u'^2 + v'^2)^{1/2} = (2E)^{1/2}$, from runs with $F = 0.8$ and $A = 0.8, 1.2, 1.6$ and 2.0 (with $f = 10^{-4} \text{ s}^{-1}$). The case with $A = 0.8$ is in regime S3, and hence the energy of the perturbation grows with time. $A = 1.2$ is in regime S2. At times when the perturbation and equilibrium velocities are closely parallel or antiparallel (e.g. initially, and again each π/f thereafter), the energy grows, but generally it decays and the model approaches the equilibrium solution. $A = 1.6$ and 2.0 are both in regime S1, and the energy of the perturbation decays monotonically with time in both cases. The time-scale for the energy to decrease to $1/e$ of its original value is rather shorter (at $\simeq 5000 \text{ s}$) in the run with $A = 2$ than that ($\simeq 8500 \text{ s}$) with $A = 1.6$. This is consistent with Eq. (13), arising primarily from the larger value of Fr_c/Fr^e with $A = 2$. In the limit of $(Fr_c/Fr^e)^2 \gg 1$ (which would require larger A with $F = 0.8$, but could, for example, be achieved even for small A with $F \lesssim 0.3$), the timescale approaches $1/(2fA)$.

5. RELEVANCE AND IMPLICATIONS FOR NWP AND CLIMATE MODELLING

Although the flow-blocking scheme is in practice implemented in a 3D model, simple considerations, involving an advection velocity and the time-scale for the 1D model to come to equilibrium, suggest that the studied equilibrium is a relevant one for NWP and climate models. More details are given in the Appendix. However, the implications of the 1D results still depend crucially on what parts of the (A, F) parameter space are populated in practice in the full 3D models. This is investigated below using diagnostics from a case-study performed with the Met Office global forecast model.

A one-day forecast has been rerun from the operational analysis valid at 1200 UTC on 11 January 2003. It used the current operational forecast resolution of $0.55^\circ \times 0.83^\circ$, which equates to a resolution of about 60 km. Diagnostics required to calculate A and F were output every 6 hours. For consistency with the operational implementation of the Webster *et al.* scheme, these calculations used $h = 2.5 \sigma$ (where σ is the standard deviation of the subgrid orography), $Fr_c = 2$ and N was taken to be the average value of the Brunt–Väisälä frequency between the surface and h . For simplicity, the wind speed at the model level above $\max(h, 500 \text{ m})$ was used as a surrogate for u_g in the calculation of F . Also, in the calculation of $A (= aN/fh)$, a was defined to be $a = \hat{K}^{-1} \sigma_{xx}$, where $\hat{K}^{-1} = 10^5 \text{ m}$, i.e. just the x-component of the squared gradient fields was used.

Figure 5 shows the global distribution of F at 12 UTC on 12 January 2003, i.e. at the end of the forecast period. The main feature to note is that the value of F is primarily determined by the value of h . Thus, the smallest values of F occur over the major orographic massifs, which is where h is largest. The diurnal cycle in F in these regions (not shown) is relatively weak. Elsewhere, where h is smaller, F is generally in

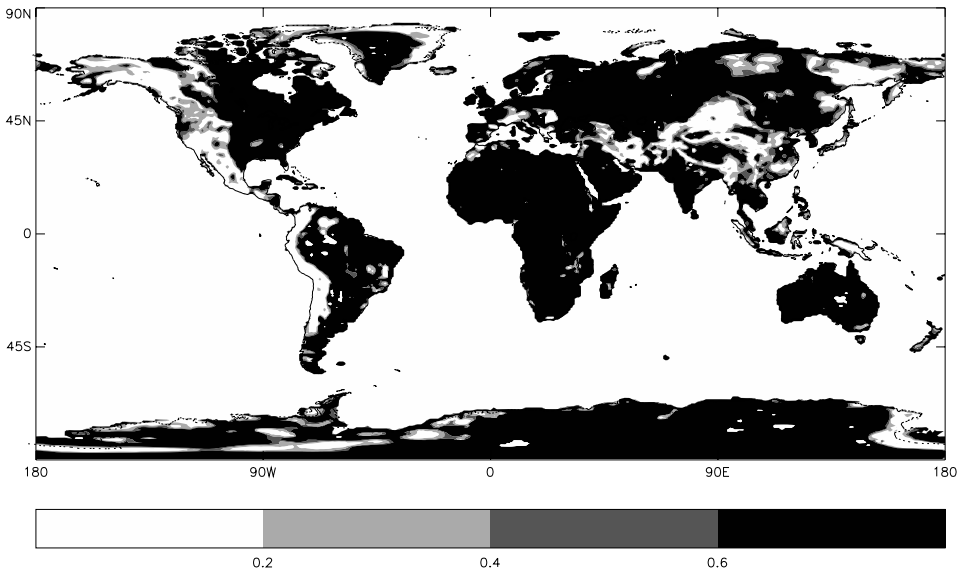


Figure 5. The geographical distribution of F over land, as derived from the forecast valid at 12 UTC on 12 January 2003. All values of $F < 0.2$ are unshaded, whilst all values of $F > 0.6$ are shaded black.

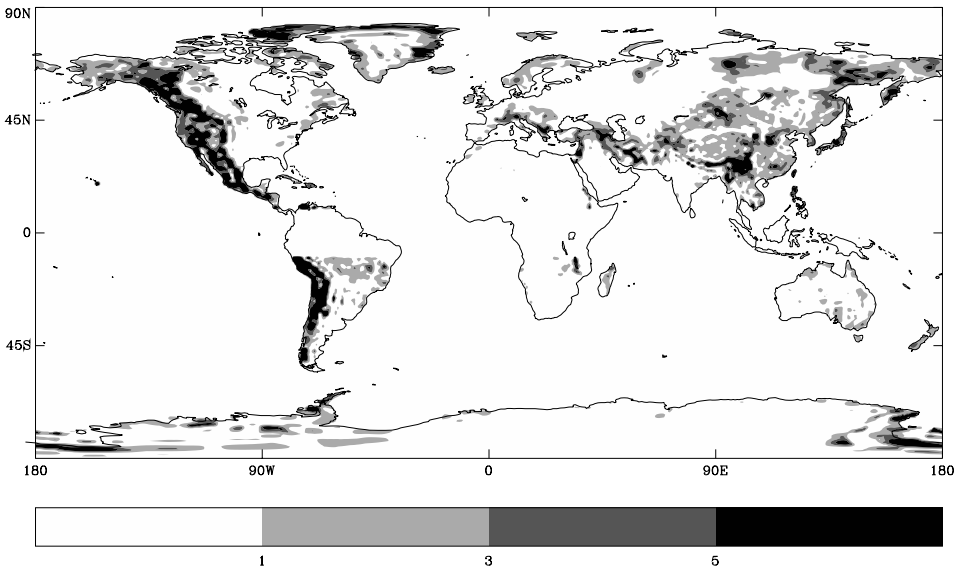


Figure 6. As Fig. 5, but showing A over land. All values of $A < 1$ are unshaded, whilst all values of $A > 5$ are shaded black. The plotting of A within 10° of the equator has been suppressed because the diagnosed values are very large since here f is very small.

excess of 0.6. However, in these regions of small h , the diurnal variation of F is much larger. This is because, where h is small, changes in boundary-layer stability may have a much greater influence on N . Thus, for example, the small (night-time) values seen over central Australia in Fig. 5 are replaced by large values during the daytime (e.g. at 00 UTC, not shown).

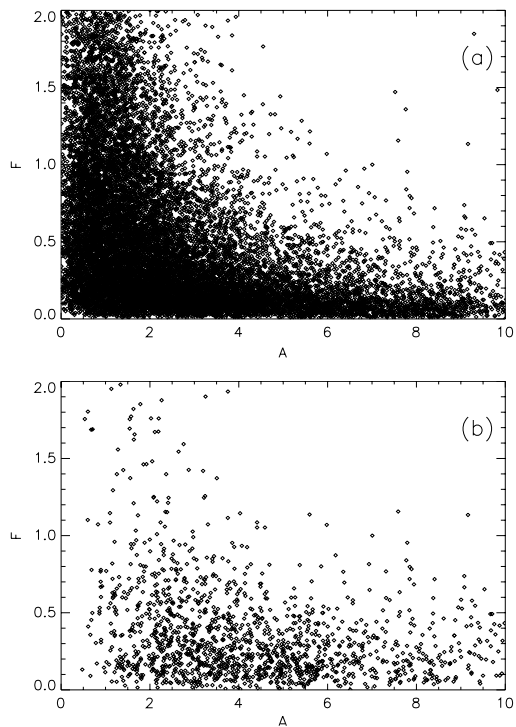


Figure 7. Scatter diagrams showing F against A for the 12 UTC on 12 January 2003 forecast for (a) all land points and (b) all points with $\tau_0 > 1 \text{ N m}^{-2}$. Note that the region of parameter space shown is larger than that shown in Fig. 1.

Figure 6 shows the distribution of A for the same time as Fig. 5. It is again evident that the geographical distribution is closely tied to the major massifs, with the largest values of A (between 1 and 10) occurring over them. This indicates that the increase of $a = \hat{K}^{-1}\sigma_{xx}$ over major orography dominates over the decrease in h^{-1} . At small h points, a similar diurnal cycle in A to that in F is evident from inspecting the values of A at other times through the day. The cycle in the two fields is out of phase, however, because A is proportional to N whereas F is inversely proportional to N . As already mentioned, the diurnal cycle is weak where h is large, and so it has little effect on the points we are most interested in.

The behaviour of the parametrization depends on both the value of F and the value of A and so, to investigate this behaviour, Fig. 7(a) plots all the values of F shown in Fig. 5 against all the values of A shown in Fig. 6. It is evident that the majority of points have small values of F and/or small values of A , with the highest density of points occurring where both F and A are small. A comparison of this distribution with the solutions shown in Fig. 1 indicates that there are very few points in the part of parameter space where multiple solutions are obtained. Hence we conclude that the existence of this regime is not a significant issue in practice.

Fig. 7(b) shows only those points with $\tau_0 > 1 \text{ N m}^{-2}$. These relatively large stresses will in general occur in regions of significant orography. Focusing on this subset of points eliminates many of those with large values of F , and the majority of these points have $F \lesssim 0.4$ and $2 \lesssim A \lesssim 6$. They therefore lie in regime S1 of Fig. 1, in which we expect a stable equilibrium solution. However, both in this plot and, to a greater extent,

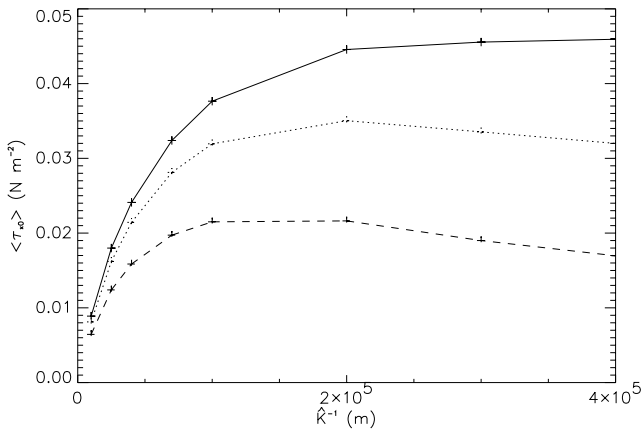


Figure 8. The variation with \hat{K}^{-1} (in the forecasts valid at 12 UTC on 12 January 2003) of the global average of the component of the surface stress in the direction of the local geostrophic wind (solid line). Dotted line: contribution to the average stress of those points for which $A > 1$ and $F < 1$ in the run with $\hat{K}^{-1} = 10^5$ m. Dashed line: contribution to the average stress of those points for which $A > 2$ and $F < 0.5$ in the run with $\hat{K}^{-1} = 10^5$ m.

in the full distribution of Fig. 7(a), there are a significant number of points in regimes S2 and S3 in which we expect the 1D equilibrium solution to be unstable. This is potentially worrying numerically, although as yet we have not seen any evidence of problems in the full model. The numerical instability essentially results from the blocking drag decreasing with increasing wind speed (and vice versa) when the Froude number is close to unity. One possibility is that the full system is stabilized by the presence of the boundary-layer scheme which does have a drag which increases monotonically with increasing wind speed. Consistent with this hypothesis, restricting the distributions to points in which the blocking drag is greater than the boundary-layer drag significantly reduces the number of points in this regime (not shown). The same restriction has little impact at low F , as in these cases the blocking drags dominate over those from the boundary-layer scheme.

As the points with the largest stresses typically have $F \lesssim 0.4$, the drag associated with orographic flow blocking tends to dominate over that associated with propagating gravity waves. Most of these points have A greater than the A_c value of around unity. Hence, for these points we may expect that increasing A by increasing the tuning coefficient \hat{K}^{-1} will not increase the component of the stress in the direction of the geostrophic wind. To investigate whether there is any evidence of this occurring in the full model, a set of seven additional forecasts has been performed with the value of \hat{K}^{-1} varied from its standard value of 10^5 m.

The solid line in Fig. 8 shows the variation with \hat{K}^{-1} of the global average of $\tau_{\alpha 0}$, the component of the surface blocking stress in the direction of the local geostrophic wind. The stress increases, but progressively more slowly, as \hat{K}^{-1} increases. However, the globally averaged stress is still increasing in the forecast with the largest \hat{K}^{-1} , presumably because the increase in stress at the many points with $A < A_c$ continues to outweigh the decrease in stress for those points with $A > A_c$. If only the contribution of those points with A close to or greater than A_c is considered, then a decrease in stress, as \hat{K}^{-1} increases, does become evident. This can be seen in the dotted line in Fig. 8, which show the contributions to the global averages of those points which in the operational run ($\hat{K}^{-1} = 10^5$ m) have $A > 1$ and $F < 1$. Increasing \hat{K}^{-1} beyond

2×10^5 m causes the average stress at these points to start to decrease. With slightly more restrictive criteria ($A > 2$ and $F < 0.5$ in the operational run), the average stress is actually a maximum at the operational value of $\hat{K}^{-1} = 10^5$ m, and decreases if \hat{K}^{-1} is either increased or decreased.

6. CONCLUSIONS

A simple 1D model has been used to help to understand the behaviour of the Webster *et al.* (2003) orographic flow-blocking scheme. This framework allows feedback of the parametrized stress on the mean wind. A surprisingly complex behaviour for an apparently simple scheme is revealed, with equilibrium stresses often very different to those that would be obtained without the feedback, and with the possibility of multiple as well as unstable solutions.

The key non-dimensional parameters that control the character of the solution have been identified. These are $F = Fr_g / Fr_c$, the ratio of a Froude number based on the geostrophic wind speed to the critical value, and $A = aN / (fh)$, a measure of the strength of the blocking. Diagnosis of these quantities from a global forecast run has shown that the most significant orography tends to have $F \lesssim 0.4$ (and so blocking drag dominates over wave drag) and $A \gtrsim 1$. In this regime the analysis indicates that the feedbacks are strong enough that increasing the tuning coefficient a will actually decrease the stress in the direction of the geostrophic wind. It has been shown that the results of the full model are consistent with this prediction.

Very few points lie in the part of parameter space which permits multiple equilibria and so the existence of this region does not appear to be a significant issue in practice. However, there are a significant number in the region in which the blocking scheme alone would give unstable equilibria. It has been speculated that the presence of the boundary-layer scheme in the full model may stabilize the solution.

While some of the details of the results will be specific to the Webster *et al.* scheme, other aspects are expected to be more generally applicable. For example, the schemes of Lott and Miller (1997) and Scinocca and McFarlane (2000) also have stresses in the blocked layer which depend on winds within the blocked layer. They will therefore be subject to similar feedbacks, and off-line (fixed wind) assessments or calibrations of the different schemes against observational or model data may give misleading results. It is suggested that understanding the properties of, and differences between, the different schemes in the present simple framework will be a useful precursor to taking advantage of any future data to discriminate between them. Extending the analyses to include a boundary-layer scheme would also be very valuable, both because of the specific concern about the stability of the solution, and also more generally because of evidence of strong interactions between flow-blocking and boundary-layer schemes (Beljaars 2001). This work could help understand the interaction (and might reveal clearly unphysical behaviour). At the same time, further idealized simulations similar to those presented in Ólafsson and Bougeault (1997) but covering a wider parameter space would be extremely useful in providing a further ‘truth’ against which the 1D simulation results could be evaluated.

APPENDIX

In order to obtain an estimate for the length-scale to adjust to equilibrium after a change in the strength of parametrized blocking, linearized horizontal advection terms ($u^e \partial u' / \partial x + v^e \partial u' / \partial y$) and ($u^e \partial v' / \partial x + v^e \partial v' / \partial y$) can be introduced on the left-hand

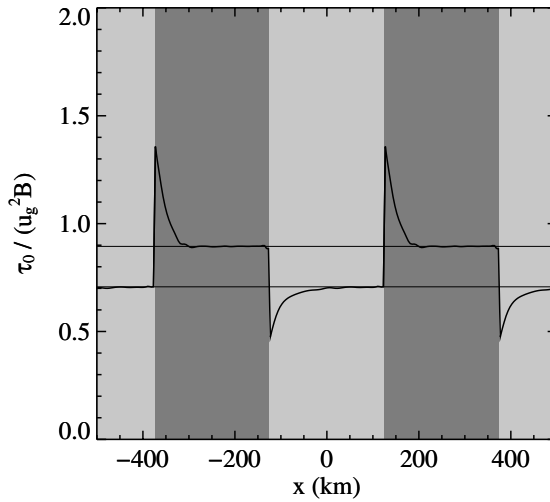


Figure A.1. Normalized surface stress as a function of position in a two-dimensional BLASIUS model run with $u_g = 10 \text{ m s}^{-1}$, $f = 10^{-4} \text{ s}^{-1}$, $F = 0$ and alternate 250 km bands with $A = 1$ and $A = 2$. The dark shading indicates locations with $A = 2$, and the lighter shading indicates $A = 1$. The light horizontal lines show the equilibrium solutions in these two regions.

sides of Eqs. (11) and (12) respectively. Combining the two equations as before, and considering the steady-state solution in the $F \ll 1$ limit, leads to

$$u^e \frac{\partial E}{\partial x} + v^e \frac{\partial E}{\partial y} = -2fAE. \quad (\text{A.1})$$

For a case with the strength of blocking changing in the x -direction, this leads to a decay scale of $l = l_x = u^e / (2fA)$. Note that, inevitably, this is just the time-scale for adjustment in the 1D problem (section 4) multiplied by the advection velocity u^e . The longest length-scale that can be obtained will be if the variation is in the direction of the equilibrium wind, so that s^e is the relevant advection velocity. In this case the length-scale is $l = l_w = s^e / (2fA)$. Both l_x and l_w will decrease with increasing A , both due to the direct effect on the time-scale, and also due to the decrease in the advection velocity. Using the equilibrium result for s^e / u_g leads to

$$\left. \begin{aligned} l_x &= \frac{(u_g/f)}{2A(1+A^2)}, \\ l_w &= \frac{(u_g/f)}{2A(1+A^2)^{1/2}}. \end{aligned} \right\} \quad (\text{A.2})$$

For $u_g = 10 \text{ m s}^{-1}$ and $f = 10^{-4} \text{ s}^{-1}$, this gives $l_x = 80, 25$ and 5 km , and $l_w = 89, 35$ and 11 km for $A = 0.5, 1.0$ and 2.0 , respectively.

In order to further examine the adjustment to equilibrium, the Webster *et al.* (2003) parametrization was included in a free-slip, 2D version of the BLASIUS model of Wood and Mason (1993). The value of A was made a function of streamwise position and the model was run to equilibrium for various combinations of parameters. The results for the adjustment length-scales were found to be qualitatively consistent with those predicted by the simple theory described above. Quantitatively there were some discrepancies (presumably associated with the neglect of nonlinear effects, vertical advection and pressure perturbations in the theory), although the diagnosed length-scales were always

within a factor of two of (and smaller than) the predicted ones. The example shown in Fig. A.1 is for a case with $u_g = 10 \text{ m s}^{-1}$, $f = 10^{-4} \text{ s}^{-1}$, $F = 0$ and alternate 250 km bands with $A = 1$ and $A = 2$. The adjustment of the surface stress to its equilibrium value over each band can be seen, with the adjustment scale being shorter on moving to the $A = 2$ bands.

These findings are reassuring in terms of the relevance of the 1D equilibrium solutions for NWP and climate models. For the choice of $u_g = 10 \text{ m s}^{-1}$ and $f = 10^{-4} \text{ s}^{-1}$, they suggest that $A \gtrsim 1$ will lead to equilibrium being approached on scales comparable to or smaller than the typical size of typical climate model grid boxes (100 km or more). Similarly, solutions in global NWP models with grid spacings of several tens of kilometres will be close to equilibrium if $A \gtrsim 2$. As we have seen, this requirement will be satisfied over most significant orography. Furthermore, even for many cases (e.g. with bigger u_g/f or smaller A) where the adjustment was insufficiently rapid for equilibrium to be reached on the scale of an NWP or climate grid box, it seems likely that the behaviour of the equilibrium solution will retain some qualitative relevance.

ACKNOWLEDGEMENT

The authors would like to acknowledge the valuable contributions of Nigel Wood to this work.

REFERENCES

- | | | |
|------------------------------------------------------------|------|---------------------------------------------------------------------------------------------------------------------------------------------------------------------------------------------------------------------------|
| Beljaars, A. C. M. | 2001 | 'Issues in boundary layer parametrization for large-scale models'. In proceedings of seminar on Issues in parametrization of subgrid processes, ECMWF, Reading, UK |
| Kim, Y.-J., Eckermann, S. D. and Chun, H.-Y. | 2003 | An overview of the past, present and future of gravity-wave drag parametrization for numerical climate and weather prediction models. <i>Atmos.–Ocean</i> , 41 , 65–98 |
| Lott, F. and Miller, M. J. | 1997 | A new subgrid-scale orographic drag parametrization: its formulation and testing. <i>Q. J. R. Meteorol. Soc.</i> , 123 , 101–127 |
| McFarlane, N. A. | 1987 | The effect of orographically excited gravity wave drag on the circulation of the lower stratosphere and troposphere. <i>J. Atmos. Sci.</i> , 44 , 1775–1800 |
| Ólafsson, H. and Bougeault, P. | 1997 | The effect of rotation and surface friction on orographic drag. <i>J. Atmos. Sci.</i> , 54 , 193–210 |
| Palmer, T. N., Shutts, G. J. and Swinbank, R. | 1986 | Alleviation of a systematic westerly bias in general circulation and numerical weather-prediction models through an orographic gravity wave drag parametrization. <i>Q. J. R. Meteorol. Soc.</i> , 112 , 1001–1039 |
| Scinocca, J. F. and McFarlane, N. A. | 2000 | The parametrization of drag induced by stratified flow over anisotropic orography. <i>Q. J. R. Meteorol. Soc.</i> , 126 , 2353–2393 |
| Webster, S., Brown, A. R., Cameron, D. R. and Jones, C. P. | 2003 | Improving the representation of orography in the Met Office Unified Model. <i>Q. J. R. Meteorol. Soc.</i> , 129 , 1989–2010 |
| Wood, N. and Mason, P. J. | 1993 | The pressure force induced by neutral, turbulent flow over hills. <i>Q. J. R. Meteorol. Soc.</i> , 119 , 1233–1267 |